Using Tidally-Driven Elastic Strains to Infer Regional Variations in Crustal Thickness at Enceladus

Alexander Berne[1], Mark Simons[1], James T. Keane[2], Ryan S. Park[2]

[1]California Institute of Technology, Pasadena, CA 91125 USA

[2]Jet Propulsion Laboratory, California Institute of Technology, Pasadena, CA 91109 USA

Key Points:

- Variations in ice shell (i.e., crustal) thickness are crucial for understanding the thermodynamics and habitability of Enceladus.
- We develop a new method to infer spatially-varying crustal thickness using measurements of tidally-driven elastic strain.
- Using our method, we demonstrate recoveries of crustal thickness variations to within < 0.2 km error over length scales greater than 60 km.

Corresponding author: Alexander Berne, `aberne@caltech.edu`

Abstract

Constraining the spatial variability of the thickness of the ice shell of Enceladus (i.e., the crust) is central to our understanding of its thermodynamics and habitability. In this study, we develop a new methodology to infer regional variations in crustal thickness using measurements of tidally-driven elastic strain. As proof of concept, we recover thickness variations from synthetic finite-element models of the crust subjected to diurnal eccentricity tides. We demonstrate recovery of crustal thickness to within ~ 2 km of true values with < 0.2 km error over spherical harmonic degrees $l \leq 12$ (corresponding to half-wavelengths ≥ 60 km). Our computed uncertainty is significantly smaller than the inherent ~ 10 km ambiguity associated with inferring variations in crustal thickness solely from gravity and topography measurements. We therefore conclude that measuring elastic strain provides a relatively robust approach for probing crustal structure at Enceladus.

Plain Language Summary

Inferences of the thickness of Enceladus's ice shell – or crust – can provide valuable insights for our understanding the potential habitability and thermodynamics of this moon of Saturn. In this work, we develop a new method to infer regional variations in crustal thickness at Enceladus using measurements of deformation caused by tidal interactions with Saturn. Using models of Enceladus's ice shell, we demonstrate that we can recover crustal thickness with a deviation of ~ 2 km relative to input values. Our approach to infer crustal thickness could complement traditional methods that rely solely on analyzing gravity and surface topography to constrain crustal structure at the satellite.

1 Introduction

Enceladus, a small moon of Saturn, is a geologically active and potentially habitable ocean world (e.g., Porco et al., 2006; Postberg et al., 2009). Enceladus possesses both highly cratered landscapes and regions with active resurfacing (e.g., the South Polar Terrain or SPT) (Yin & Pappalardo, 2015; Schenk et al., 2018). Based on an incomplete spherical harmonic degree $l = 3$ gravity and topography fields derived primarily from three spacecraft flybys, the SPT is believed to have significantly thinner crust ($\sim 4 - 14$

km) relative to a mean crustal thickness ($\sim 20 - 40$ km) (Nimmo et al., 2011; Iess et al., 2014; Hemingway et al., 2018). The SPT also possesses four large-scale fractures (informally known as 'Tiger Stripes'; Porco et al., 2006). Cryovolcanic jets along the Tiger Stripes are believed to supply material from a subsurface ocean (Thomas et al., 2016; Iess et al., 2014) to a water-ice plume which exhibits diurnal variations in activity (e.g., Ingersoll et al., 2020). Diurnal eccentricity tides may correspondingly regulate crustal dynamics by cyclically deforming Enceladus over its 32.9 hr orbital period (Souček et al., 2016).

Characterizing the spatial variability of crustal thickness at Enceladus is crucial for studying the satellite's thermodynamics and habitability. It is believed that basal heating (and melting) of the ice shell maintains variations in crustal thickness over geologic timescales (Čadek et al., 2019; Hemingway & Mittal, 2019). Additionally, for an ice shell that exhibits Airy isostatic compensation of surface topography, the amplitudes of crustal thickness variations are sensitive to the density of the ocean (Hemingway & Matsuyama, 2017). Determination of ocean density enables identification of differences between ocean compositions predicted from analyzing plume material and actual ocean compositions (Fifer et al., 2022). Knowledge of ocean composition (and in particular the abundances of compounds NaCl, CO_2, H_2, NH_4, and CH_4) in turn constrain the pH, salinity, and availability of chemical energy for metabolic reactions at Enceladus (Postberg et al., 2011; Glein et al., 2018). Characterizing crustal thickness at Enceladus also constrains plausible escape pathways of ocean material (e.g., local refreezing in thinned regions of the ice shell; Čadek et al., 2019) and modes of intra-crustal processing of material sourced from the ocean (Kite & Rubin, 2016; Ingersoll & Nakajima, 2016).

Several methods have been proposed to infer spatially variable crustal thickness at Enceladus. Measurements of gravity and topography can provide constraints on variations in crustal thickness across regional spatial scales (i.e., $l = 2 - 20$) (e.g., Ermakov et al., 2021). However, previous geodetic studies at Enceladus (Iess et al., 2014; McKinnon, 2015; Hemingway & Mittal, 2019) predict a wide possible range of crustal thickness values across regional spatial scales (e.g., $4 - 14$ km, or ~ 10 km near the South Pole). Ambiguity in determinations of crustal thickness from existing geodetic surveys arises primarily from uncertain estimates of the impact of ocean and crustal densities on Enceladus's gravity field (Hemingway & Mittal, 2019). Efforts to more precisely determine thickness using libration measurements (e.g., Thomas et al., 2016; Van Hoolst et al., 2016) or observations of local lithospheric flexure induced by the presence of surface topogra-

phy (e.g., Giese et al., 2008) constrain values only at long ($l = 2$) or short ($l > 20$) spatial scales, respectively.

We develop a new method for inferring crustal thickness at Enceladus using measurements of elastic strain across regional spatial scales. From Hooke's law, strain along a loaded 1D system scales linearly with local stiffness (Figure 1). For an elastic layer, both layer thickness and elastic moduli influence the tendency for a medium to resist deformation in response to an applied force. We therefore anticipate that changes in the strain field produced by diurnal tides at a given location in Enceladus's crust will exhibit a linear relationship with variations in the local elastic thickness. We note that ice deformation on Enceladus is mostly elastic over 32.9 hr timescales (Shaw, 1985; Wahr et al., 2006; Neumeier, 2018). Thus, inferences of elastic thickness from diurnal tides closely approximate (to within $< 0.2\%$) true crustal thickness at Enceladus. Further details are described in the Supplementary text S1.5 of Berne et al. (2023).

Gradients in material properties, such as crustal thickness and elastic moduli, induce additional complexity in the response of a 2D layer to applied tractions (Hsu et al., 2011 cf. Equation 4). We refer to this phenomenon as the 'gradient' effect, which we illustrate in Figure 1. Crustal thickness gradients can lead to biased estimates of crustal thickness when using a linear (one-to-one) interpretation of strain fields, particularly when gradients are high (e.g., when variations in crustal thickness are present at short wavelengths). Analytic models of diurnal tides at Enceladus are unable to predict deformation caused by short-wavelength variations in crustal thickness (Beuthe, 2018; Rovira-Navarro et al., 2020). However, numerical Finite Element Models (FEMs) can accurately simulate deformation of ice shell geometries that incorporate variations in crustal thickness across a wide range of spatial scales (Souček et al., 2016; Behounkova et al., 2017; Souček et al., 2019; Berne et al., 2023a).

Here, we introduce an approach to determine crustal thickness at Enceladus through the application of Hooke's law to tidally-induced elastic strains (Section 2). Our approach utilizes numerical techniques to iteratively minimize differences between measured crustal strains and those predicted using FEMs of spatially heterogeneous ice shells subject to tidal loading. To account for potential gradient effects, our FEMs incorporate variations in crustal thickness at length scales down to ~ 25 km or spherical harmonic degree $l \sim 60$. As proof of concept, we demonstrate recovering thickness using elastic strains from
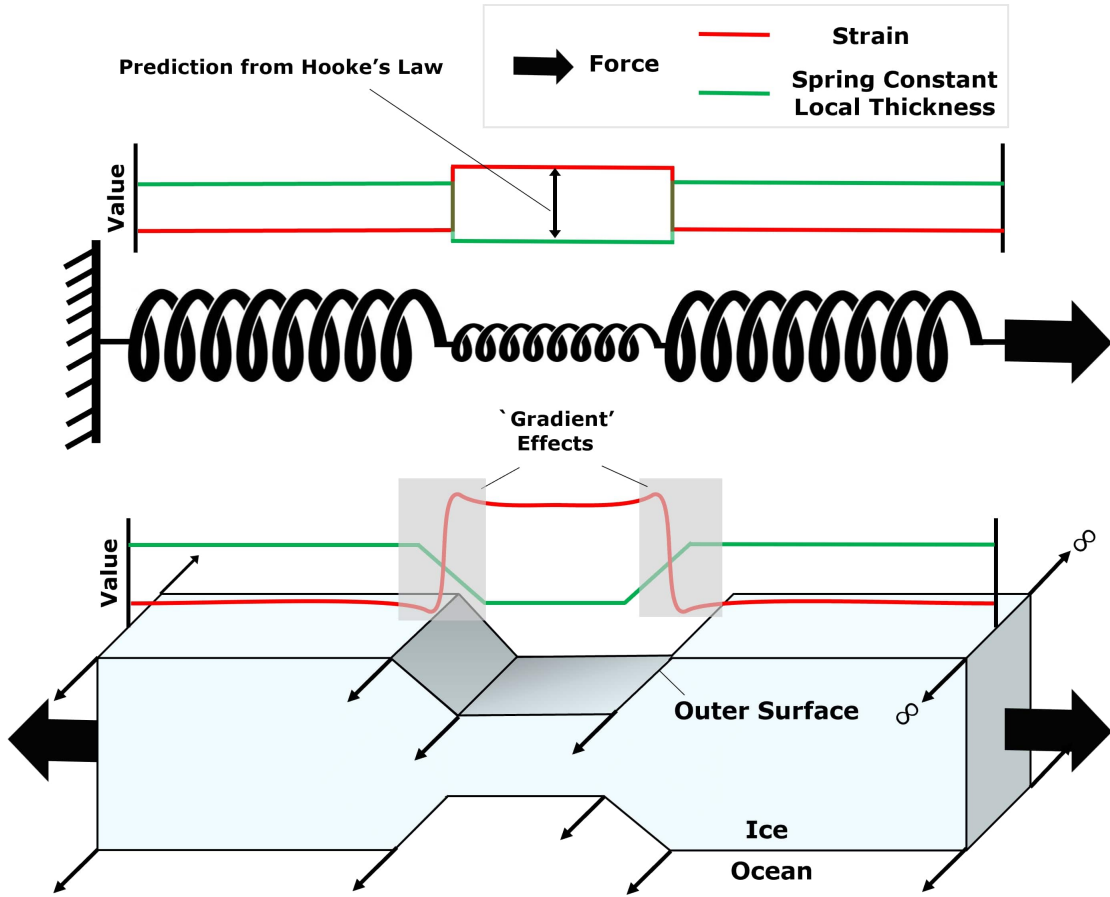
Figure 1. Crustal strain correlates with ice shell thickness. Top Panel: Example 1D elastic structure (i.e., springs in series) subject to an axial load. Hooke's law predicts that strain is relatively higher where springs have lower stiffness (i.e., smaller spring constants). Bottom Panel: Analogous 2D elastic layer subject to a transverse load. In this case, local layer thickness modulates the effective stiffness (and strain) of the medium. We expect that measurements of strain at the outer surface of the crust (labelled) permit inferences of local thickness at Enceladus. Shaded regions denote locations where 'gradient effects' impact inferences of local thickness from strain fields.

108   a synthetic model of Enceladus's ice shell using our methodology (Section 3). We assess

109   uncertainty by comparing the discrepancy between thicknesses that are input into the

110   synthetic models with thicknesses recovered from those models. We conclude by address-

111   ing the utility of using imaging geodesy (e.g., Interferometric Synthetic Apreture Radar)

112   to carry out the strain measurements required to recover crustal thickness variations at

113   Enceladus (Section 4).

2   Methods

2.1   Input Model Specification

116   We first construct a spherically symmetric model geometry that is broadly consis-

117   tent with the elastic structure of the crust of Enceladus. Building on the methodology

118   discussed in Berne et al., (2023) (section 2.1), we start with a hollow shell with prescribed

119   outer radius R and uniform thickness $\tilde{D}$ (see Supplementary Table S1 for chosen values

120   for parameters used throughout this work). Using the software package CUBIT (Skroch

121   et al., 2019; CoreForm, 2020), we mesh our geometry with tetrahedral elements and as-

122   sign a uniform shear modulus G and a bulk modulus value μ. We ignore the potential

123   impact of viscous strain (Wahr et al., 2009). We also account for self-gravitational ef-

124   fects and ignore inertial forces for our analysis. Elastic deformation of the core is expected

125   to be several orders of magnitude smaller than elastic deformation of the ice shell (Schu-

126   bert et al., 2007). We therefore treat the core as a rigid body for simulations.

127   For our analysis, we construct a synthetic 'true' crustal thickness model by mod-

128   ifying the surface and ice-ocean boundary of our spherically symmetric geometry. $D^{true}(\boldsymbol{\Omega})$

129   represents the spatially variable thickness of the outer ice shell of our synthetic model

130   where $\boldsymbol{\Omega}$ is the position variable comprising the co-latitude longitude pair (θ, ϕ) in a body-

131   fixed reference frame. Note that we can write the quantity $D^{true}(\boldsymbol{\Omega})$ as a sum over or-

132   thonormal spherical harmonic basis functions $Y_{lm}(\boldsymbol{\Omega})$ scaled by coefficients d_{lm}^{true} (where

133   l and m denote spherical harmonic degree and order):

$$D^{true}(\boldsymbol{\Omega}) = \sum_{l=0}^{\infty} \sum_{m=-l}^{l} d_{lm}^{true} Y_{lm}(\boldsymbol{\Omega}) \tag{1}$$

135   We generate d_{lm}^{true} up to $l = 60$ by compensating observed surface topography using a

136   modified form of Airy isostasy (Hemingway & Matsuyama, 2017). Further details of our

137 procedure to generate thickness variations in the synthetic model are given in Supple-

138 mentary S1.1.

2.2 Tidal Loading

140 Following the formulation described in Supplementary section S1.1 of Berne et al.,

141 (2023), we apply forces associated with the driving potential produced by time-dependent

142 diurnal eccentricity tides $V(r, \theta, \phi, t)$ (to the first order in eccentricity) to model geome-

143 tries (Murray & Dermott, 1999):

$$
\begin{aligned}
V(r, \theta, \phi, t) = r^2 \omega^2 e \cdot (\sin(\omega t) \, \mathrm{P}_{22}(\mu) \sin 2\phi ... \\
... + \frac{3}{4}\cos(\omega t) \, (\mathrm{P}_{22}(\mu) \cos 2\phi - 2 \, \mathrm{P}_{20}(\mu)))
\end{aligned}
\tag{2}
$$

145 In Equation 2, ω is Enceladus's orbital angular velocity, e is the body's orbital eccen-

146 tricity, and r is radial position in a body-fixed reference frame. Time $t = 0, \frac{2\pi}{\omega}$ corre-

147 sponds to orbital periapse. $P_{20}(\mu)$ and $P_{22}(\mu)$ are associated Legendre Functions with

148 the nested function $\mu = \cos(\theta)$. We use the 3D FEM code PyLith (Aagaard et al., 2007)

149 for simulations. PyLith is a well-established geodynamic modelling tool which allows for

150 complex bulk rheology and geometrical meshes. We have modified PyLith for modeling

151 full spheres in a no-net-rotation/translation reference frame with central time-dependent

152 body forces appropriate for eccentricity tides (See also section 2.2 of Berne et al., 2023a).

2.3 Strain Computation

154 Following the methodology described in Tape et al. (2009) (cf. Equation 20), for

155 a deforming quasi-spherical body with a linear isotropic elastic rheology, we can com-

156 pute components of the horizontal strain rate tensor $\boldsymbol{\epsilon}$ at the surface according to:

$$
\epsilon_{ij} = \frac{1}{R}
\begin{bmatrix}
-\frac{3\mu-2G}{3\mu+4G}\left(2v_r + \frac{dv_\theta}{d\theta} + \cdots \right. & & \\
\left. \cdots v_\theta \cot\theta + \csc\theta \frac{dv_\phi}{d\phi}\right) & 0 & 0 \\
0 & v_r + \frac{dv_\theta}{d\theta} & \frac{1}{2}\left(-v_\phi \cot\theta + \csc\theta \frac{dv_\theta}{d\phi} + \frac{dv_\phi}{d\theta}\right) \\
0 & \frac{1}{2}\left(-v_\phi \cot\theta + \csc\theta \frac{dv_\theta}{d\phi} + \frac{dv_\phi}{d\theta}\right) & v_r + v_\theta \cot\theta + \csc\theta \frac{dv_\phi}{d\phi}
\end{bmatrix}
\tag{3}
$$

158 where quantities $v_r, v_\theta,$ and v_ϕ denote surface velocities in positive radial, co-latitude,

159 and longitude directions. To compute v_r, v_θ and v_ϕ, we difference FEM displacement fields

160 between 180 consecutive time points over the tidal cycle ($t = 0$ to $t = \frac{2\pi}{\omega}$ in Equation 2).

Subtracting the dilatation of the strain tensor ϵ_h from diagonal components of ϵ_{ij} in Equation 3 permits computation of the horizontal deviatoric strain rate tensor $\tilde{\epsilon}_{ij}$:

$$\tilde{\epsilon}_{ij} = \epsilon_{ij} - \epsilon_h \delta_{ij} \tag{4}$$

where δ_{ij} is the kronecker delta. We evaluate ϵ_h by averaging diagonal components of ϵ_{ij} in Equation 3:

$$\epsilon_h = \frac{\epsilon_{11} + \epsilon_{22} + \epsilon_{33}}{3} \tag{5}$$

For convenience, we seek to parameterize strain rate at the surface of our models using a scalar quantity, here called $E(\boldsymbol{\Omega})$ (see section 2.1 for the definition of $\boldsymbol{\Omega}$). Using matrix components $\tilde{\epsilon}_{ij}$ in Equation 4, we define $E(\boldsymbol{\Omega})$ as the time-averaged 2nd invariant of the deviatoric horizontal strain rate:

$$E(\boldsymbol{\Omega}) = \frac{\omega}{2\pi} \int_0^{\frac{2\pi}{\omega}} |\tilde{\epsilon}_{11}\tilde{\epsilon}_{22} + \tilde{\epsilon}_{22}\tilde{\epsilon}_{33} + \tilde{\epsilon}_{11}\tilde{\epsilon}_{33} - \tilde{\epsilon}_{23}\tilde{\epsilon}_{32}| \, dt \tag{6}$$

By definition, the strain invariants do not depend on our coordinate system. The 2nd invariant of the horizontal deviatoric horizontal strain rate (i.e., as opposed to 1st or 3rd invariants, non-deviatoric strain rate, etc.) is especially sensitive to variations in elastic layer thickness and yields relatively high signal-to-noise ratios for recoveries of crustal thickness at Enceladus (see next section).

3 Results

3.1 Initial Crustal Thickness Recovery

We perform an iterative analysis to recover thickness from strain fields. $D^n(\boldsymbol{\Omega})$ and $E^n(\boldsymbol{\Omega})$ respectively denote thickness and strain fields evaluated at a given iteration number n. To assess the discrepancy between thicknesses that are input and recovered from models for each iteration, we compute the mismatch $\delta D^n(\boldsymbol{\Omega})$ between $D^n(\boldsymbol{\Omega})$ and $D^{true}(\boldsymbol{\Omega})$:

$$\delta D^n(\boldsymbol{\Omega}) = D^n(\boldsymbol{\Omega}) - D^{true}(\boldsymbol{\Omega}) \tag{7}$$

We initially (i.e., $n = 0$) recover crustal thickness $D^0(\boldsymbol{\Omega})$ using 'observed' strains (i.e., $E^{obs}(\boldsymbol{\Omega})$) extracted from our FEM with thickness $D^{true}(\boldsymbol{\Omega})$. Hooke's law predicts that

thickness is inversely proportional to strain in a 2D elastic medium subject to a transverse load (as previously shown in Figure 1). It is therefore reasonable to assume the following linear relationship between $E^{obs}(\mathbf{\Omega})$ and $D^0(\mathbf{\Omega})$:

$$\frac{D^0(\mathbf{\Omega})}{\tilde{D}} = \kappa(\mathbf{\Omega})\frac{E^{Base}(\mathbf{\Omega})}{E^{obs}(\mathbf{\Omega})} \tag{8}$$

where $\kappa(\mathbf{\Omega})$ is a linear transfer function and $E^{Base}(\mathbf{\Omega})$ is strain evaluated on a spherically symmetric Enceladus with uniform thickness $\tilde{D}$. $\kappa(\mathbf{\Omega})$ accounts for the differential $E(\mathbf{\Omega})$ produced by thickness variations (of constant amplitude) located at different angular positions $\mathbf{\Omega}$ across Enceladus. Since the amplitude of the tidal forcing varies over a predominantly long-wavelength $E(\mathbf{\Omega})$ pattern (i.e., $l = 2$; see Equation 2) we can account for the impact of $\kappa(\mathbf{\Omega})$ by applying a high-pass filter to strain fields (for details, see Supplementary S1.2).

Figure 2 shows snapshots of $D^{true}(\mathbf{\Omega})$, $E^{obs}(\mathbf{\Omega})$, $D^0(\mathbf{\Omega})$, and $\delta D^0(\mathbf{\Omega})$ from our analysis. For visualization, we plot the logarithm of $E^{obs}(\mathbf{\Omega})$ normalized by $E^{Base}(\mathbf{\Omega})$ (i.e., $\widehat{E}^{obs}(\mathbf{\Omega})$):

$$\widehat{E}^{obs}(\mathbf{\Omega}) = \log\frac{E^{obs}(\mathbf{\Omega})}{E^{Base}(\mathbf{\Omega})} \tag{9}$$

As expected, patterns of $\widehat{E}^{obs}(\mathbf{\Omega})$ correlate with patterns of $D^{true}(\mathbf{\Omega})$. Computed $\widehat{E}^{obs}(\mathbf{\Omega})$ fields reflect regional thinning at North and South poles, a relatively thicker crust at low latitudes, and the significant asymmetry in crustal thinning between northern and Southern hemispheres visible in $D^{true}(\mathbf{\Omega})$. Recovered crustal thickness patterns, $D^0(\mathbf{\Omega})$, more closely match $D^{true}(\mathbf{\Omega})$ than do $\widehat{E}^{obs}(\mathbf{\Omega})$. Slight differences between $D^{true}(\mathbf{\Omega})$ and $D^0(\mathbf{\Omega})$ (i.e., $\delta D^0(\mathbf{\Omega})$ in Equation 7) appear to localize near regions with short-wavelength variations in crustal thickness (i.e., high contour density) consistent with the influence of gradient effects on our analysis. In particular, we significantly overestimate crustal thickness ($\delta D^0(\mathbf{\Omega})$ values up to 25 km) along several prominent ridges over the Trailing and Southern Hemispheres.

3.2 Gradient Effect Correction

We iteratively adjust the amplitude of crustal thicknesses $D^n(\mathbf{\Omega})$ to minimize differences between strain produced by models with recovered crustal thickness fields $E^n(\mathbf{\Omega})$
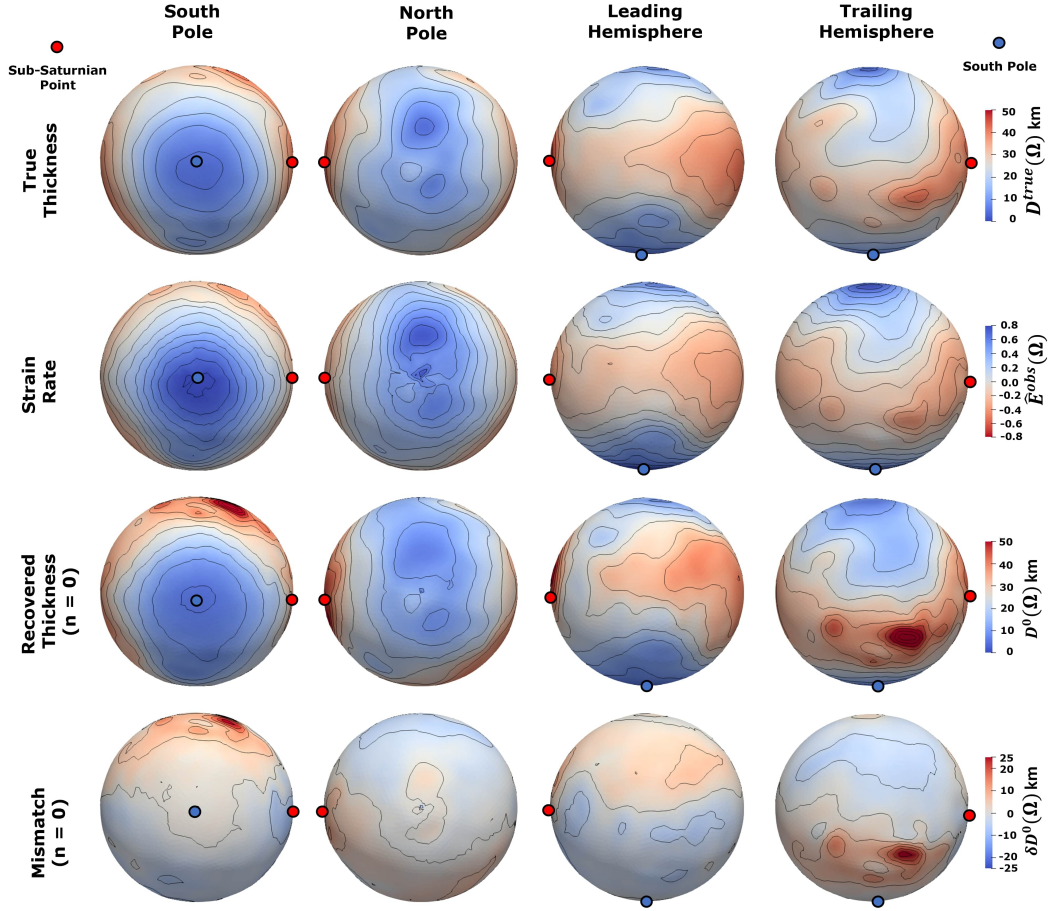
Figure 2. Snapshots of model input crustal thickness $D^{true}(\mathbf{\Omega})$ (first row), the simulated 2nd invariant of time-averaged horizontal deviatoric strain rate $\widehat{E}^{obs}(\mathbf{\Omega})$ (see Equations 6 and 9) (second row), recovered crustal thickness $D^0(\mathbf{\Omega})$ evaluated from Equation 8 (third row), and mismatch between input and recovered thickness $\delta D^0(\mathbf{\Omega})$ (see Equation 7) for our initial recovery of crustal thickness ($n = 0$) viewed facing Southern, Northern, Leading, and Trailing hemispheres. See Supplementary S1.1 for description of how synthetic 'true' crustal thickness models were constructed. Plotted contours denote colorscale intervals of 0.05 (for $\widehat{E}^{obs}(\mathbf{\Omega})$ fields) and 5 km (for $D^n(\mathbf{\Omega})$ and $\delta D^n(\mathbf{\Omega})$ fields). Images are orthographic projections with labelled sub-Saturnian point and South Pole locations.

214   and 'true' strain $E^{obs}(\mathbf{\Omega})$ (see section 2.4). We define a cost function evaluated at a given

215   iteration $\xi^E(n)$ as the integrated square of the difference between $E^{obs}(\mathbf{\Omega})$ and $E^n(\mathbf{\Omega})$:

$$\xi^E(n) = \int (E^n(\mathbf{\Omega}) - E^{obs}(\mathbf{\Omega}))^2 \cdot d\mathbf{\Omega} \tag{10}$$

217   For comparison to $\xi^E(n)$, we additionally track the integrated square of the difference

218   between true and recovered thicknesses $\xi^D(n)$:

$$\xi^D(n) = \int (D^n(\mathbf{\Omega}) - D^{true}(\mathbf{\Omega}))^2 \cdot d\mathbf{\Omega} \tag{11}$$

220   We expect that the extent to which gradient effects distort strain fields at a given loca-

221   tion scales with the magnitude of the local gradient in crustal thickness $||\nabla D^n(\mathbf{\Omega})||$. We

222   therefore update $D^n(\mathbf{\Omega})$ to $D^{n+1}(\mathbf{\Omega})$ for iterations $n > 0$ following:

$$\log\left(\frac{D^{n+1}(\mathbf{\Omega})}{D^n(\mathbf{\Omega})}\right) = \eta(n) \cdot ||\nabla D^n(\mathbf{\Omega})|| \cdot M(\mathbf{\Omega}) \tag{12}$$

224   where $\eta(n)$ is the learning rate and $M(\mathbf{\Omega})$ is a spatially variable prefactor defined as:

$$M(\mathbf{\Omega}) = \kappa(\mathbf{\Omega})^{-1}\frac{E^n(\mathbf{\Omega}) - E^{obs}(\mathbf{\Omega})}{E^{Base}(\mathbf{\Omega})} \tag{13}$$

226   We incorporate $M(\mathbf{\Omega})$ into Equation 12 to ensure modifications to $D^n(\mathbf{\Omega})$ only correct

227   for over- (under-) predictions of local thickness in locations with reduced (elevated) $E^n(\mathbf{\Omega})$

228   relative to $E^{obs}(\mathbf{\Omega})$. We also update $\eta(n)$ between iterations following an adaptive al-

229   gorithm to ensure $\xi^E(n)$ converges to a local minimum (Barzilai & Borwein, 1988). Note

230   that we can expand $D^n(\mathbf{\Omega})$ for each iteration in Equation 12 into spherical harmonic func-

231   tions:

$$D^n(\mathbf{\Omega}) = \sum_{l=0}^{\infty} \sum_{m=-l}^{l} d_{lm}^n Y_{lm}(\mathbf{\Omega}) \tag{14}$$

233   where d_{lm}^n are spherical harmonic coefficients. We can examine mismatch in the spec-

234   tral domain (i.e., spectral power) by evaluating the root-mean-square (RMS) of thick-

235   ness coefficients d_{lm}^n in Equation 14 and d_{lm}^{true} in Equation 1 over l (i.e., d_l^n and d_l^{true} re-

236   spectively) as well as the RMS percentage difference between coefficients d_{lm}^n and d_{lm}^{true}

237   (i.e., δd_l^n):

$$d_l^n = \left(\frac{1}{2l+1} \sum_m (d_{lm}^n)^2 \right)^{1/2} \tag{15a}$$

$$d_l^{true} = \left(\frac{1}{2l+1} \sum_m (d_{lm}^{true})^2 \right)^{1/2} \tag{15b}$$

$$\delta d_l^n = \left(\frac{1}{2l+1} \sum_m \left(\frac{d_{lm}^n - d_{lm}^{true}}{d_{lm}^{true}} \right)^2 \right)^{1/2} \cdot 100\% \tag{15c}$$

Figure 3 shows snapshots of $D^{true}(\mathbf{\Omega})$, $D^1(\mathbf{\Omega})$, $\delta D^1(\mathbf{\Omega})$, $D^{12}(\mathbf{\Omega})$, and $\delta D^{12}(\mathbf{\Omega})$ (i.e., see Equations 7 and 12). In addition, Figure 4 shows $\delta D^n(\mathbf{\Omega})$, d_l^n, d_l^{true}, and δd_l^n for iterations $n = 0$, 1, and 12 (see Equation 15). The non-zero $\delta D^0(\mathbf{\Omega})$ observed in Figure 3 drives broad differences between recovered and true spectral powers d_l^0 and d_l^{true} as well as non-zero values of δd_l^0 across all wavelengths. Iterating through our analysis once ($n = 1$) reduces $\delta D^1(\mathbf{\Omega})$ to < 20 km along prominent ridges over the Trailing and Southern Hemispheres, lessens the mismatch between d_l^1 and d_l^{true} curves, and diminishes δd_l^1 values across all wavelengths. Further changes to crustal thickness for iterations $n = 1$ – 12 reduces δd_l^{12} across longer wavelengths (i.e., $l \leq 12$) and reduces $\delta D^{12}(\mathbf{\Omega})$ to ~ 2 km (1σ confidence).

Figure 4 presents the strain mismatch cost function, $\xi^E(n)$, and integrated thickness mismatch, $\xi^D(n)$, for iterations $n = 0 - 15$. Our results demonstrate a slight increase in $\xi^E(n)$ from iterations $n = 12 - 15$, while $\xi^D(n)$ (as well as $\delta D^n(\mathbf{\Omega})$ and δd_l^n) values remain largely unchanged after $n \sim 12$. Bayesian approaches (e.g., Cawley & Talbot, 2007) enable determination of a suitable cutoff iteration number to avoid over-fitting strain fields (i.e., in the absence of knowledge of 'true' thickness) but are beyond the scope of the current study.

4 Discussion and Conclusion

We examine the relationship between tidally-driven elastic strains and spatially variable crustal thickness at Enceladus. Results show a broad correlation between strain fields and crustal thickness across the moon (see Figure 2). Gradient effects modulate strain patterns (see Figures 3 and 4) with diminishing impact at longer wavelengths (see Figure 4). Our approach permits final recoveries of crustal thickness to within ~ 2 km of input values (1σ confidence) with minimal error (< 0.2 km) across spatial wavelengths $l \leq 12$ (i.e., corresponding to a half-wavelength of ~ 60 km; see Figure 4, iteration $n = 12$).
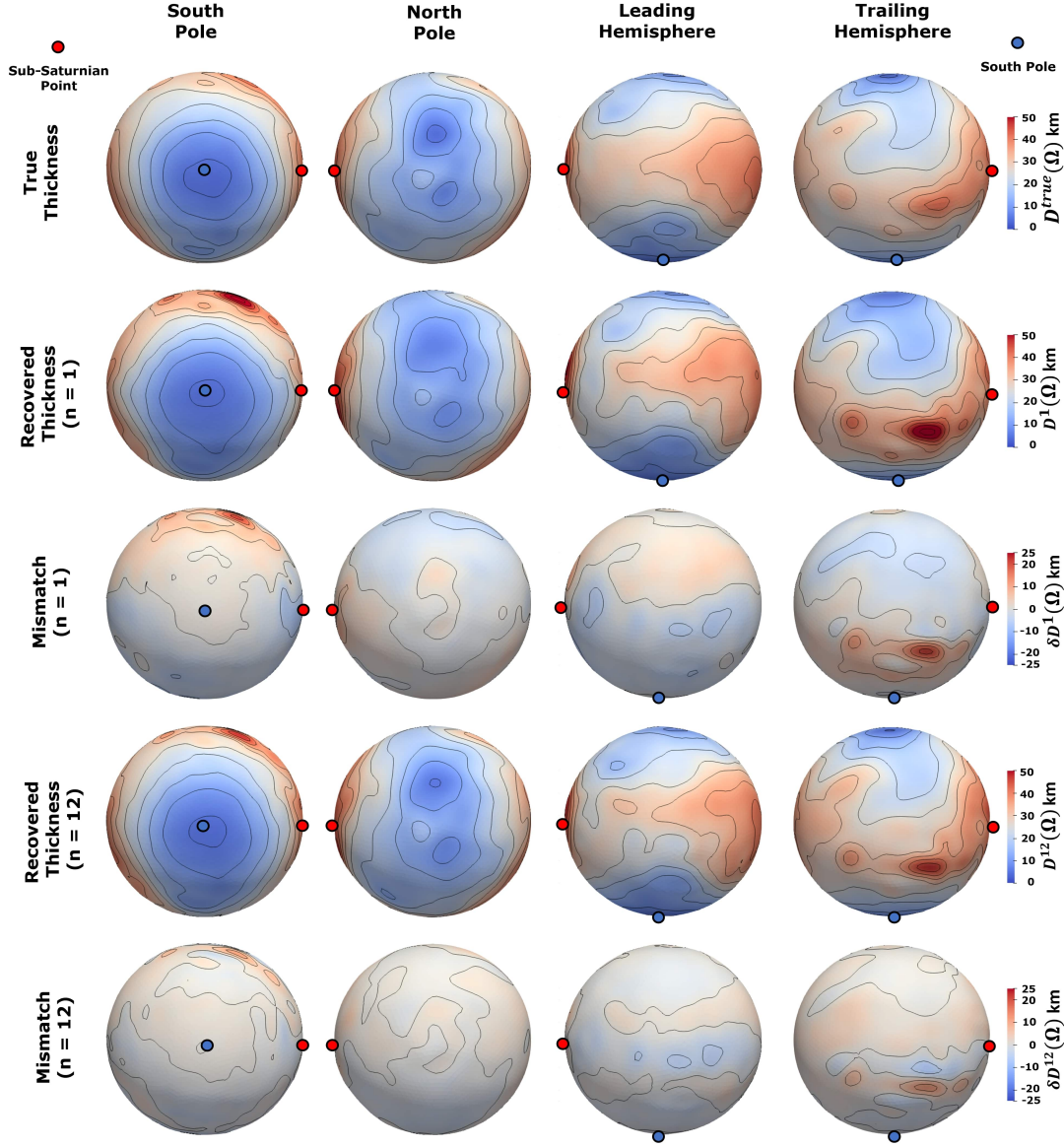
Figure 3. Snapshots of input crustal thickness $D^{true}(\mathbf{\Omega})$ (first row), recovered thickness following $n = 1$ iteration $D^1(\mathbf{\Omega})$ (second row), mismatch between model and input crustal thickness following $n = 1$ iteration $\delta D^1(\mathbf{\Omega})$ (see Equations 7) (third row), recovered crustal thickness following $n = 12$ iterations $D^{12}(\mathbf{\Omega})$ (fourth row), and mismatch between model and input crustal thickness following $n = 12$ iterations $\delta D^{12}(\mathbf{\Omega})$ (fifth row) viewed facing the Southern, Northern, Leading, and Trailing hemispheres. Plotted contours denote colorscale intervals of 5 km for $\delta D^n(\mathbf{\Omega})$ and $D^n(\mathbf{\Omega})$ fields. Images are orthographic projections with labelled sub-Saturnian point and South Pole locations.
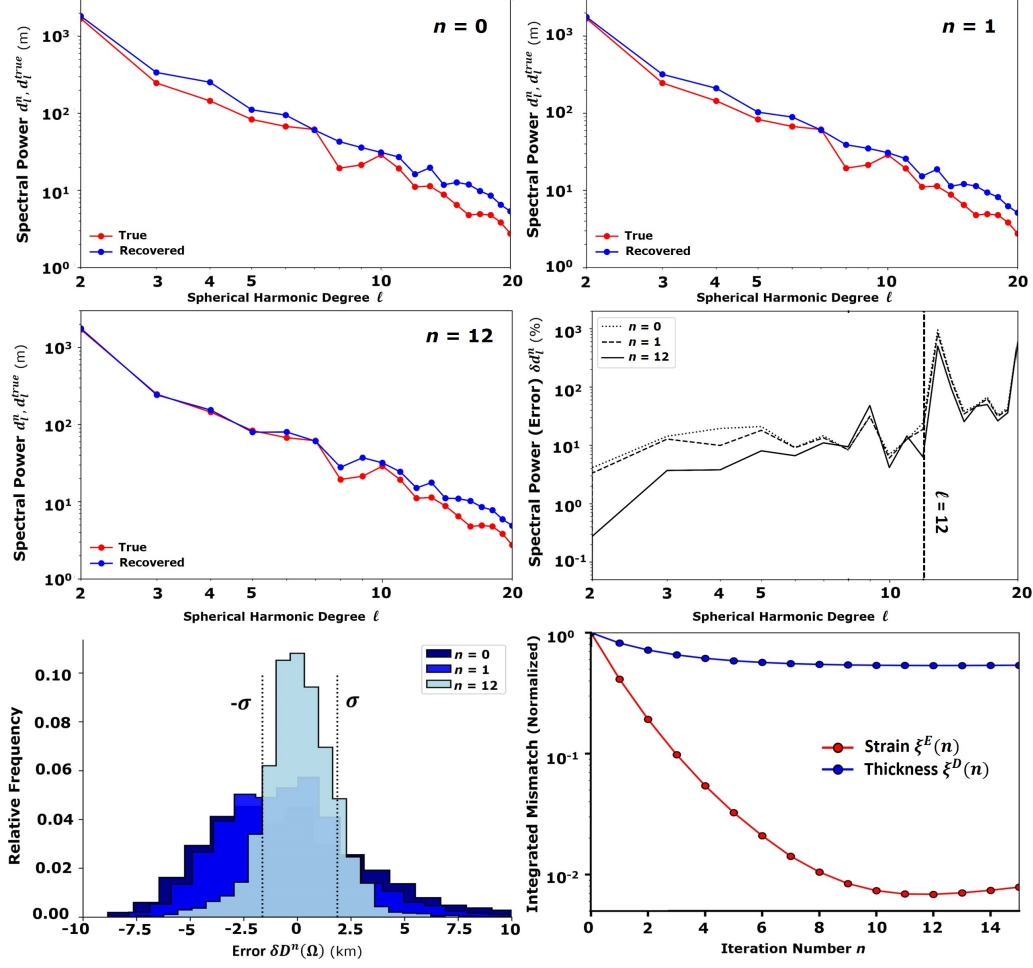
Figure 4. Analysis of mismatch between thickness fields that are input and recovered from models at a given iteration n using our analysis. Upper and center left panels show d_l^n and d_l^{true} evaluated for spherical harmonic degrees $l = 2 - 20$. d_l^n and d_l^{true} denote the spectral power of input and recovered thicknesses (see Equation 15ab; $d_l^n = d_l^{true}$ denotes a perfect recovery of crustal thickness). Note that the difference between d_l^n and d_l^{true} decreases (i.e., error decreases) after several iterations (i.e., increasing values of of n). Center right panel shows δd_l^n evaluated for spherical harmonic degrees $l = 2 - 20$. δd_l^n is the spectral power of mismatch between input and recovered thicknesses at spherical harmonic degree l (see Equation 15c; $\delta d_l^n = 0$ denotes a perfect recovery of crustal thickness). Note that δd_l^n decreases (i.e., error decreases) after several iterations (i.e., increasing values of of n). Vertical dash-dot lines at $l = 12$ marked for reference. Lower left panel shows a histogram of $\delta D^n(\mathbf{\Omega})$ values (evaluated at FEM node locations) across recovered models for $n = 0$, 1, and 12. 1σ for the $n = 12$ case plotted as vertical dash-dot lines for reference. Lower right panel shows the cost function $\xi^E(n)$ (see Equation 10) and integrated thickness mismatch $\xi^D(n)$ (see Equation 11), normalized relative to the maximum value, for iterations $n = 0 - 15$. X-axes of upper and center panels are plotted in $\log_{10}$ scale.

Our approach to correct for gradient effects minimally reduces error in crustal thickness estimates for $l > 12$ (see Figure 4). Note that length scales $l = 12 - 20$ ($\sim 60 - 40$ km) approach the upper limit of input crustal thickness values for models (~ 50 km, see Figures 2 and 3). We therefore suspect that tidal strain exhibits a generally more complex relationship with the amplitude of thickness variations than that considered by our approach (see Equations 8 and 12) at length scales that are comparable to the crustal thickness. To further examine the scaling relationship between crustal thickness and the accuracy of recoveries of crustal thickness, we repeat our analysis with mean crustal thickness $\tilde{D} = 50$ km corresponding with maximum thickness values ~ 100 km. In this case, crustal thickness estimates become significantly less accurate (i.e., exhibit > 10 % error) across wavelengths $l \geq 8$ (i.e., ≤ 90 km; for further details see Supplementary S2.1).

Our analysis assumes a-priori knowledge of $\tilde{D}$ (mean crustal thickness). $\tilde{D}$ is a crucial parameter for acquiring an initial estimate of variations in crustal thickness (i.e., $D^0(\boldsymbol{\Omega})$, see Equation 8). Measuring the amplitude of long-wavelength diurnal deformation (e.g., Love numbers k_{20} and h_{20}) at Enceladus (Beuthe, 2018; Berne et al., 2023a) likely enables determinations of $\tilde{D}$ (see Figure 4 in Berne et al., 2023a) to within $< 20\%$ of the true value, which is comparable to errors for estimates of spatially variable crustal thickness using our approach at long wavelengths (see Figure 4). Moreover, our iterative analysis is expected to correct for over-(under-) predictions of strain due to excessively low (high) initial estimates of $\tilde{D}$ (see Equation 13).

While fractures are assumed to have no impact on the recovery of crustal thickness in our initial analysis, faults such as Tiger Stripes and other potential weak zones (i.e., chasma and Circum-Tectonic Boundaries; Yin & Pappalardo, 2015) may concentrate strain under tidal loading. FEMs enable us to compute the deformation caused by both fractures and variations in crustal thickness, allowing for easy future modification of our methodology to examine the impact of fractures on strain fields at Enceladus (For more information, see Berne et al. (2023) on the 'weak zone' formulation).

In this study, we treat the single case of a crustal structure with Airy isostatic compensation of surface topography (Hemingway & Matsuyama, 2017). However, future investigations could employ Monte Carlo methods to examine whether the derived ~ 2 km error from our analysis holds for recoveries of thickness on a range of different scenario crustal models of Enceladus. In addition, modifying our approach to consider the

full surface strain field (Tape et al., 2009) or static gravity and topography data (Hemingway & Mittal, 2019) could yield estimates of crustal thickness that are more precise than results presented in Figures 2 – 4. Although beyond the scope of this study, such analyses are crucial to fully evaluate the reliability of our methodology for recovering 3D crustal structure from real geodetic measurements at Enceladus.

In the future, geodetic imaging techniques such as Interferometric Synthetic Apreture Radar (InSAR) measurements of ground deformation from orbiting platforms (e.g., Simons & Rosen, 2015) could enable the analysis described in this work. Our results indicate that the presence of crustal thickness variations generates maximum peak-to-peak horizontal and radial displacements of approximately $\pm$1-10 cm over the tidal cycle (see also Figures 2 and 3 of Berne et al., 2023a). These values exceed the demonstrated sensitivity of InSAR measurements to ground displacement (e.g., Simons & Rosen, 2015). Moreover, our analysis can be extended to calculate the relationship between strain and thickness at discrete time points, such as during repeat InSAR passes. As such, we expect that InSAR measurements would provide key insights into the interior structure of Enceladus and thus to our assessment of the moon's habitability.

Open Research

The data used in this study were generated using the software package PyLith (Aagaard et al., 2007; Aagaard et al., 2022). PyLith is an open-source finite element code for modeling geodynamic processes and is available on GitHub and Zenodo repositories

(Aagaard et al., 2022). The specific PyLith version used in this study was v2.2.2. PyLith input files (including sample surface topography data), post-processing scripts, and selected output files for this work are available on (Berne, 2023b; `https://zenodo.org/record/7996766`). The mesh geometries utilized in this study were created using CUBIT (v15.2), a node-locked licensed software which is available through the developer Sandia National Laboratories (Skroch et al., 2019; CoreForm, 2020).

References

Aagaard, B., Williams, C., & Knepley, M. (2007). PyLith: A Finite-Element Code for Modeling Quasi-Static and Dynamic Crustal Deformation. *Eos*, *88(52)*.

Aagaard, B., Williams, C., & Knepley, M. (2022). PyLith: A Finite-Element Code for Modeling Quasi-Static and Dynamic Crustal Deformation. *geodynamics/pylith v2.2.2 (v2.2.2) [Computer software]. Zenodo,https://doi.org/10.5281/zenodo.3269486*, .

Barzilai, J., & Borwein, J. M. (1988). Two-point step size gradient methods. *IMA Journal of Numerical Analysis*, *8*. doi: 10.1093/imanum/8.1.141

Behounkova, M., Soucek, O., Hron, J., & Cadec, O. (2017). Plume activity and tidal deformation on enceladus influenced by faults and variable ice shell thickness. *Astrobiology*, *17*(9). doi: 10.1089/ast.2016.1629

Berne, A. (2023). *acberne/Berne_2023_Pylith_Input_Files_Using_Tidally_Driven_Elastic_Strains_To_Infer_Regional_Variations_in_Crustal_Thickness_at_Enceladus: Pylith input files and selected outputs for Berne et al., 2023 (v1.0.0).* `https://zenodo.org/record/7996766`, `https://doi.org/10.5281/zenodo.7996766`. Zenodo.

Berne, A., Simons, M., Keane, J., & Park, R. (2023). Inferring the mean effective elastic thickness of the outer ice shell of enceladus from diurnal crustal deformation. *Journal of Geophysical Research E: Planets*, . doi: 10.22541/essoar.167117599.96425607/v1

Beuthe, M. (2018). Enceladus's crust as a non-uniform thin shell: I tidal deformations. *Icarus*, *302*. doi: 10.1016/j.icarus.2017.11.009

Cawley, G. C., & Talbot, N. L. (2007). Preventing over-fitting during model se-

lection via bayesian regularisation of the hyper-parameters. *Journal of Machine Learning Research*, *8*.

CoreForm. (2020). "CUBIT" https://coreform.com/products/coreform-cubit/ .

Ermakov, A. I., Park, R. S., Roa, J., Castillo-Rogez, J. C., Keane, J. T., Nimmo, F., . . . Lainey, V. (2021). A recipe for the geophysical exploration of enceladus. *Planetary Science Journal*, *2*. doi: 10.3847/PSJ/ac06d2

Fifer, L., Catling, D., & Toner, J. (2022). Chemical fractionation modeling of plumes indicates a gas-rich, moderately alkaline enceladus ocean. *The Planetary Science Journal*, *3*. doi: 10.3847/PSJ/ac7a9f

Giese, B., Wagner, R., Hussmann, H., Neukum, G., Perry, J., Helfenstein, P., & Thomas, P. C. (2008). Enceladus: An estimate of heat flux and lithospheric thickness from flexurally supported topography. *Geophysical Research Letters*, *35*. doi: 10.1029/2008GL036149

Glein, C. R., Postberg, F., & Vance, S. D. (2018). *The geochemistry of enceladus: Composition and controls.* doi: 10.2458/azu_uapress_9780816537075-ch003

Hemingway, Iess, L., Tajeddine, R., & Tobie, G. (2018). The interior of enceladus. In *Enceladus and the icy moons of saturn.* The University of Arizona Press in collaboration with Lunar and Planetary Institute, Houston.

Hemingway, & Matsuyama, I. (2017). Isostatic equilibrium in spherical coordinates and implications for crustal thickness on the Moon, Mars, Enceladus, and elsewhere. *Geophysical Research Letters*, *44*(15). doi: 10.1002/2017GL073334

Hemingway, & Mittal, T. (2019). Enceladus's ice shell structure as a window on internal heat production. *Icarus*, *332*. doi: 10.1016/j.icarus.2019.03.011

Hsu, Simons, M., Williams, C., & Casarotti, E. (2011). Three-dimensional fem derived elastic green's functions for the coseismic deformation of the 2005 mw 8.7 nias-simeulue, sumatra earthquake. *Geochemistry, Geophysics, Geosystems*, *12*. doi: 10.1029/2011GC003553

Iess, L., Stevenson, D. J., Parisi, M., Hemingway, D., Jacobson, R. A., Lunine, J. I., & Tortora, P. (2014). The gravity field and interior structure of Enceladus. *Science*, *344*(6179). doi: 10.1126/science.1250551

Ingersoll, A. P., Ewald, S. P., & Trumbo, S. K. (2020). Time variability of the enceladus plumes: Orbital periods, decadal periods, and aperiodic change. *Icarus*, *344*. doi: 10.1016/j.icarus.2019.06.006

Ingersoll, A. P., & Nakajima, M. (2016). Controlled boiling on enceladus. 2. model of the liquid-filled cracks. *Icarus*, *272*. doi: 10.1016/j.icarus.2015.12.040

Kite, E. S., & Rubin, A. M. (2016). Sustained eruptions on enceladus explained by turbulent dissipation in tiger stripes. *Proceedings of the National Academy of Sciences of the United States of America*, *113*. doi: 10.1073/pnas.1520507113

McKinnon, W. B. (2015). Effect of enceladus's rapid synchronous spin on interpretation of cassini gravity. *Geophysical Research Letters*, *42*. doi: 10.1002/2015GL063384

Murray, C. D., & Dermott, S. F. (2000). *Solar System Dynamics.* doi: 10.1017/cbo9781139174817

Neumeier, J. J. (2018). Elastic constants, bulk modulus, and compressibility of h2o ice i h for the temperature range 50 k-273 k. *Journal of Physical and Chemical Reference Data*, *47*. doi: 10.1063/1.5030640

Nimmo, F., Bills, B. G., & Thomas, P. C. (2011). Geophysical implications of the long-wavelength topography of the Saturnian satellites. *Journal of Geophysical Research E: Planets*, *116*(11). doi: 10.1029/2011JE003835

Porco, Helfenstein, P., Thomas, P. C., Ingersoll, A. P., Wisdom, J., West, R., & Squyres, S. (2006). Cassini observes the active south pole of enceladus. *Science*, *311*. doi: 10.1126/science.1123013

Postberg, F., Kempf, S., Schmidt, J., Brilliantov, N., Beinsen, A., Abel, B., ... Srama, R. (2009). Sodium salts in e-ring ice grains from an ocean below the surface of enceladus. *Nature*, *459*. doi: 10.1038/nature08046

Postberg, F., Schmidt, J., Hillier, J., Kempf, S., & Srama, R. (2011). A salt-water reservoir as the source of a compositionally stratified plume on enceladus. *Nature*, *474*. doi: 10.1038/nature10175

Rovira-Navarro, M., Gerkema, T., Maas, L. R., van der Wal, W., van Ostayen, R., & Vermeersen, B. (2020). Tides in subsurface oceans with meridional varying thickness. *Icarus*, *343*. doi: 10.1016/j.icarus.2020.113711

Schenk, P. M., Clark, R. N., Howett, C. J. A., Verbiscer, A. J., & Waite, J. H. (2018). *Enceladus and the icy moons of saturn.* doi: 10.2458/azu_uapress_9780816537075

Schubert, G., Anderson, J. D., Travis, B. J., & Palguta, J. (2007). Enceladus: Present internal structure and differentiation by early and long-term radiogenic

heating. *Icarus*, *188*(2). doi: 10.1016/j.icarus.2006.12.012

Shaw, G. H. (1985). Elastic properties and equation of state of high pressure ice. *The Journal of Chemical Physics*, *84*. doi: 10.1063/1.449897

Simons, M., & Rosen, P. A. (2015). Interferometric Synthetic Aperture Radar Geodesy. In *Treatise on geophysics: Second edition* (Vol. 3). doi: 10.1016/B978-0-444-53802-4.00061-0

Skroch, M., Owen, S., Staten, M., Quadros, R., Hanks, B., Clark, B., & Stimpson, C. (2019). *CUBIT Geometry and Mesh Generation Toolkit 15.4 User Documentation.*

Souček, O., Běhounková, M., Čadek, O., Hron, J., Tobie, G., & Choblet, G. (2019). Tidal dissipation in Enceladus' uneven, fractured ice shell. *Icarus*, *328*. doi: 10.1016/j.icarus.2019.02.012

Souček, O., Hron, J., Běhounková, M., & Čadek, O. (2016). Effect of the tiger stripes on the deformation of Saturn's moon Enceladus. *Geophysical Research Letters*, *43*(14). doi: 10.1002/2016GL069415

Tape, C., Musé, P., Simons, M., Dong, D., & Webb, F. (2009). Multiscale estimation of gps velocity fields. *Geophysical Journal International*, *179*. doi: 10.1111/j.1365-246X.2009.04337.x

Thomas, P. C., Tajeddine, R., Tiscareno, M. S., Burns, J. A., Joseph, J., Loredo, T. J., & Porco, C. (2016). Enceladus's measured physical libration requires a global subsurface ocean. *Icarus*, *264*. doi: 10.1016/j.icarus.2015.08.037

Van Hoolst, T., Baland, R. M., & Trinh, A. (2016). The diurnal libration and interior structure of enceladus. *Icarus*, *277*. doi: 10.1016/j.icarus.2016.05.025

Wahr, Selvans, Z. A., Mullen, M. E., Barr, A. C., Collins, G. C., Selvans, M. M., & Pappalardo, R. T. (2009). Modeling stresses on satellites due to nonsynchronous rotation and orbital eccentricity using gravitational potential theory. *Icarus*, *200*(1). doi: 10.1016/j.icarus.2008.11.002

Yin, A., & Pappalardo, R. T. (2015). Gravitational spreading, bookshelf faulting, and tectonic evolution of the South Polar Terrain of Saturn's moon Enceladus. *Icarus*, *260*. doi: 10.1016/j.icarus.2015.07.017

Čadek, O., Souček, O., Běhounková, M., Choblet, G., Tobie, G., & Hron, J. (2019). Long-term stability of enceladus' uneven ice shell. *Icarus*, *319*. doi: 10.1016/j.icarus.2018.10.003